Berry curvature of interacting bosons in a honeycomb lattice

Yun Li,[1] Pinaki Sengupta,[2,3] George G. Batrouni,[3,4,5,6] Christian Miniatura,[3,4,6,7] and Benoît Grémaud[3,6,7,8]
[1]*Centre for Quantum and Optical Science, Swinburne University of Technology, Melbourne, Victoria, 3122, Australia*
[2]*School of Physical and Mathematical Science, Nanyang Technological University, 21 Nayang Link, 637371 Singapore*
[3]*MajuLab, CNRS-UNS-NUS-NTU International Joint Research Unit UMI 3654, Singapore*
[4]*INLN, Université de Nice-Sophia Antipolis, CNRS; 1361 route des Lucioles, 06560 Valbonne, France*
[5]*Institut Universitaire de France, 103 boulevard Saint Michel, 75005 Paris, France*
[6]*Centre for Quantum Technologies, National University of Singapore, 2 Science Drive 3, 117542 Singapore*
[7]*Department of Physics, National University of Singapore, 2 Science Drive 3, 117542 Singapore*
[8]*Laboratoire Kastler Brossel, UPMC-Sorbonne Universités, CNRS, ENS-PSL Research University, Collège de France, 4 Place Jussieu, 75005 Paris, France*
(Received 17 June 2015; published 6 October 2015)

We consider soft-core bosons with on-site interaction loaded in the honeycomb lattice with different site energies for the two sublattices. Using both a mean-field approach and quantum Monte Carlo simulations, we show that the topology of the honeycomb lattice results in a nonvanishing Berry curvature for the band structure of the single-particle excitations of the system. This Berry curvature induces an anomalous Hall effect when driving the system out of equilibrium. It is seen by studying the time evolution of a wave packet, namely, a superfluid ground state in a harmonic trap, subjected either to a constant force (Bloch oscillations) or to a sudden shift of the trap center.

DOI: 10.1103/PhysRevA.92.043605 PACS number(s): 03.75.−b, 67.85.Bc, 67.85.Hj, 05.30.Rt

I. INTRODUCTION

Topology and gauge fields, exemplified by Chern numbers, Berry phases, Zak phase, and Berry curvatures [1–3], are key concepts at the heart of many condensed-matter phenomena [4–6]. For solid-state systems, Bloch's theorem introduces wave numbers **k** belonging to a parameter space with the topology of a torus, the Brillouin zone, and a set of periodic wave functions depending parametrically on **k** which offer natural settings for bundles and connections [7]. Recently, ultracold atomic systems have progressively and successfully confirmed their ability to mimic or emulate some paradigmatic phenomena of condensed-matter systems, in particular topological effects. Indeed one can now load independent or interacting bosons and/or fermions into two-dimensional, very well controlled, optical lattices [8–12] and one can generate carefully designed synthetic magnetic fields [13–16]. These advances pave the way to accurate cold atom experiments targeting topology-related effects such as defects [17], color superfluidity [18], momentum-space Berry curvatures [19], or quantum Hall states with strong effective magnetic fields [20–25].

Because of its remarkable low-energy electronic excitations, graphene has been the source of many key discoveries [26,27] which sparked a vivid research flow now reaching new territories as exemplified by ultracold atoms loaded in optical lattices [10,24,28–35]. In particular, the tight-binding model on the honeycomb lattice or equivalently on the brick wall lattice is well known to exhibit a Berry curvature in its band structure [25,36,37], such that the anomalous Hall effect can be observed [5,38]. In this paper, we discuss the impact on the Berry curvature of the interactions between bosons loaded in the honeycomb lattice with site energy imbalance, i.e., when the site energies of the two sublattices are different. In that case, the phase diagram depicts Mott-insulating phases at half-integer filling, a feature that is shared with the energy imbalanced square lattice. On the other hand, as we show below, the properties of the Bogoliubov excitations above the ground state are different for these two lattices: only the excitations for the honeycomb lattice depict a nonvanishing Berry curvature. This is emphasized by looking at a dynamical situation, i.e., driving the system out of equilibrium, such as the Bloch oscillations, where the anomalous Hall effect is observed.

The paper is organized as follows. In Sec. II, we introduce the model, summarize the basic properties of the energy imbalanced honeycomb lattice (in particular, the Berry curvature), and we present the two approaches used in the paper: the quantum Monte Carlo (QMC) method [39–42] and the Gutzwiller ansatz [43–45]. In Sec. III, we present our numerical results: the ground-state phase diagram and the excitations, emphasizing that they depict nonvanishing Berry curvature. In Sec. IV, we explain how to observe the anomalous Hall effect resulting from the Berry curvature in the excitations. A summary of results and conclusions is given in Sec. V.

II. MODEL

A. Single-particle Hamiltonian and Berry curvature

We start with a general bipartite lattice structure with four nearest neighbors. Each primitive unit cell contains two lattice sites A and B, as depicted in Fig. 1. The whole lattice structure can be generated by repeated translations of a unit cell along the Bravais primitive vectors

$$\boldsymbol{a}_1 = \hat{\boldsymbol{e}}_x - \hat{\boldsymbol{e}}_y \quad \text{and} \quad \boldsymbol{a}_2 = \hat{\boldsymbol{e}}_x + \hat{\boldsymbol{e}}_y, \tag{1}$$

where we have assumed the spacing between two sites in the primitive unit cell is unity. Thereby, the scales for length, momentum, and Berry curvature are set to unity. The primitive

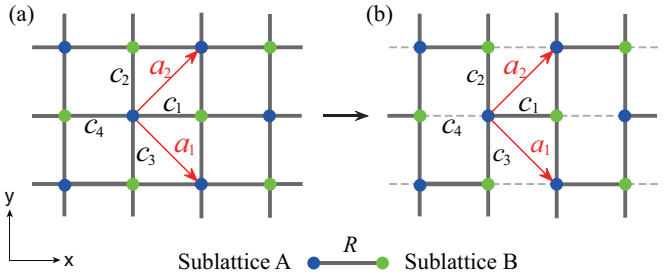

FIG. 1. (Color online) Structure of a bipartite lattice with four nearest neighbors. Sites belonging to sublattice A are represented by dark (blue) points in the figure, whereas B sites are represented by light-gray (green) points. The hopping amplitudes are all equal in (a) while in (b) the hopping term t_4 along links $\boldsymbol{c}_4$ is different from the other three near neighbor hopping terms.

reciprocal lattice vectors are

$$\boldsymbol{b}_1 = \pi(\hat{\boldsymbol{e}}_x - \hat{\boldsymbol{e}}_y) \quad \text{and} \quad \boldsymbol{b}_2 = \pi(\hat{\boldsymbol{e}}_x + \hat{\boldsymbol{e}}_y), \tag{2}$$

and fulfills the relation $\boldsymbol{a}_i \cdot \boldsymbol{b}_j = 2\pi\delta_{ij}$.

The displacements that move an A site to a neighboring B site are parametrized by bond vectors

$$\boldsymbol{c}_1 = -\boldsymbol{c}_4 = \hat{\boldsymbol{e}}_x, \quad \boldsymbol{c}_2 = -\boldsymbol{c}_3 = \hat{\boldsymbol{e}}_y. \tag{3}$$

Atoms trapped in the lattice can hop from one site to the neighboring sites with amplitudes t_ν ($\nu = 1 \ldots 4$) corresponding to the four bond vectors. In the absence of interactions, the Hamiltonian in real space reads

$$H_0 = -\sum_{\langle i,j\rangle}(t_{ij}\, b_i^\dagger b_j + t_{ij}^*\, b_j^\dagger b_i) - \mu_A \sum_{i\in A} n_i - \mu_B \sum_{j\in B} n_j, \tag{4}$$

where $t_{ij} \in \{t_1, t_2, t_3, t_4\}$, b_i is the operator annihilating one particle on lattice site i, $n_i = b_i^\dagger b_i$ is the atom number operator, and μ_A and μ_B are chemical potentials for sublattice A and B, respectively. When all hopping amplitudes t_ν are the same, Eq. (4) describes a standard square lattice. If $t_4 = 0$, the lattice becomes the brick wall lattice which is topologically equivalent to the honeycomb lattice. In this paper, all numerical results are obtained for the brick wall lattice, allowing a simpler comparison with the square lattice. Nevertheless, the properties obtained for the brick wall lattice (in particular, the topological ones) also hold for the honeycomb lattice; more precisely, some results, such as the phase diagram, are exactly the same and some results, such as the band structure and the Berry curvature, only differ in geometrical details. Using Fourier transform, we obtain the Hamiltonian in momentum space

$$H_0 = \sum_{\mathbf{k}} (b_{\mathbf{k}A}^\dagger \quad b_{\mathbf{k}B}^\dagger) \begin{pmatrix} \Delta & \Gamma_{\mathbf{k}} \\ \Gamma_{\mathbf{k}}^* & -\Delta \end{pmatrix} \begin{pmatrix} b_{\mathbf{k}A} \\ b_{\mathbf{k}B} \end{pmatrix} - \mu N, \tag{5}$$

where $\mathbf{k}$ is the Bloch wave vector, $\Delta = -(\mu_A - \mu_B)/2$, $\mu = (\mu_A + \mu_B)/2$, $N = \sum_{\mathbf{k}}(b_{\mathbf{k}A}^\dagger b_{\mathbf{k}A} + b_{\mathbf{k}B}^\dagger b_{\mathbf{k}B})$ is the total number of particles, and $\Gamma_{\mathbf{k}} = -\sum_{\nu=1}^4 t_\nu\, e^{-i\mathbf{k}\cdot\boldsymbol{c}_\nu}$. The Hamiltonian (5) has the eigenvalues

$$\epsilon_\pm(\mathbf{k}) = \pm\sqrt{\Delta^2 + |\Gamma_{\mathbf{k}}|^2} - \mu \tag{6}$$

and eigenfunctions [37]

$$|\psi_{\mathbf{k}+}\rangle = \begin{pmatrix} \cos\frac{\beta}{2} \\ \sin\frac{\beta}{2} e^{i\phi} \end{pmatrix}, \quad |\psi_{\mathbf{k}-}\rangle = \begin{pmatrix} -\sin\frac{\beta}{2} e^{-i\phi} \\ \cos\frac{\beta}{2} \end{pmatrix}, \tag{7}$$

where $\phi = -\arg\Gamma_{\mathbf{k}}$ and $\beta = \arcsin(|\Gamma_{\mathbf{k}}|/\sqrt{\Delta^2 + |\Gamma_{\mathbf{k}}|^2})$. For $\Delta = 0$, the gap between the two energy bands closes at $|\Gamma_{\mathbf{k}}| = 0$, and exhibit the so-called Dirac cone. To open a gap, one needs to imbalance the chemical potential between the A and B sites. In the following, we always consider the gapped case, i.e., $\Delta \neq 0$.

The Berry curvature for each band of the Hamiltonian (5) can be calculated as [37]

$$\Omega_\pm(\mathbf{k}) = \pm\frac{1}{2}\left(\frac{\partial\cos\beta}{\partial k_x}\frac{\partial\phi}{\partial k_y} - \frac{\partial\cos\beta}{\partial k_y}\frac{\partial\phi}{\partial k_x}\right). \tag{8}$$

Expanding the Bloch wave vector $\mathbf{k}$ over the reciprocal primitive vectors, $\mathbf{k} = \alpha_1\boldsymbol{b}_1 + \alpha_2\boldsymbol{b}_2$, we find the Berry curvature (8) can be written as follows:

$$\Omega_\pm(\mathbf{k}) = \pm\frac{1}{2}\frac{\Delta}{(\Delta^2 + |\Gamma_{\mathbf{k}}|^2)^{3/2}}\{[t_1t_3 - t_2t_4]\sin(2\pi\alpha_2) - [t_1t_2 - t_3t_4]\sin(2\pi\alpha_1)\}, \tag{9}$$

where we have assumed real values for the hopping amplitudes. For the square lattice ($t_\nu = t$), the Berry curvature is always zero, reflecting the presence of both the inversion and the time-reversal symmetry in the system. However, if one of the hopping amplitudes is different from the other three, for example $t_4 \neq t_{1,2,3}$, the symmetry under the exchange $x \to -x$ is broken. As a consequence, the system can exhibit a nonvanishing Berry curvature. In this case, as the symmetry under the exchange $y \to -y$ remains, $\beta(\mathbf{k})$ and $\phi(\mathbf{k})$ are even functions of k_y. According to Eq. (8), one can easily see that the Berry curvature should be an odd function of k_y, i.e., $\Omega_\pm(k_x, k_y) = -\Omega_\pm(k_x, -k_y)$.

In Fig. 2, we give an example of the Berry curvature in the first Brillouin zone (BZ), i.e., for $|\alpha_i| < 1/2$, calculated

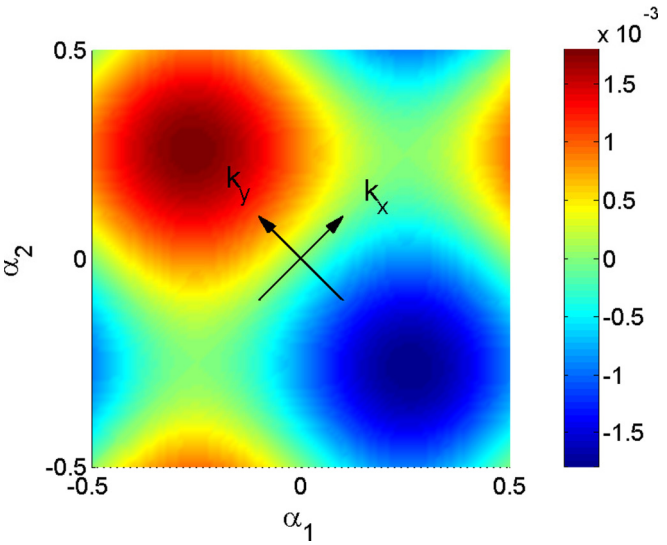

FIG. 2. (Color online) Berry curvature in the first Brillouin zone for the brick wall lattice calculated from Eq. (9). The parameters are chosen as follows: $t_{1,2,3} = t$, $t_4 = 0$, $\Delta = 5t$.

from (9) for the imbalanced brick wall lattice, i.e., $t_{1,2,3} = t$, $t_4 = 0$, and $\Delta = 5t$. Due to the time-reversal symmetry, the Berry curvature has the usual property $\Omega_\pm(-\mathbf{k}) = -\Omega_\pm(\mathbf{k})$ such that, for each band, the Chern number which is the surface integral of Berry curvature, $\gamma_\pm = \int_{\mathrm{BZ}} dS\, \Omega_\pm(\mathbf{k})$, is vanishing. This emphasizes that the bands are topologically trivial. Furthermore, due to the odd symmetry of the Berry curvature under the exchange $k_y \to -k_y$, it is also an even function of k_x, $\Omega_\pm(k_x,k_y) = \Omega_\pm(-k_x,k_y)$, as shown in Fig. 2: in the (α_1,α_2) plane, the Berry curvature is symmetric with respect to the antidiagonal $(\alpha_1,\alpha_2) \to (-\alpha_2, -\alpha_1)$ and antisymmetric with respect to the diagonal $(\alpha_1,\alpha_2) \to (\alpha_2,\alpha_1)$.

B. Numerical methods

When the interaction on a site is taken into account, the system can be described by the Bose-Hubbard Hamiltonian

$$H = H_0 + \frac{U}{2}\sum_i n_i(n_i - 1), \tag{10}$$

where H_0 is given by (4), and U is the on-site interaction strength. This is the Hamiltonian we shall investigate in this study using two complementary methods that are described below.

1. Quantum Monte Carlo

The ground state of Hamiltonian (10) can be studied using the stochastic series expansion (SSE) quantum Monte Carlo method with operator-loop updates [39–41]. The SSE is a finite-temperature QMC algorithm based on importance sampling of the diagonal matrix elements of the density matrix $e^{-\beta\mathcal{H}}$. There are no approximations beyond statistical errors. Using the operator-loop cluster update, the autocorrelation time for the system sizes we consider here is at most a few Monte Carlo sweeps for the entire range of parameter space explored. The simulations are carried out on finite lattices with L^2 sites for L up to 32 at temperatures sufficiently low in order to resolve ground-state properties of this finite system [42]. Estimates of physical observables in the thermodynamic limit are obtained from simultaneous finite-size and finite-temperature extrapolation to the $L \to \infty$, $\beta \to \infty$ limit. We consider here the soft-core boson case which allows multiple occupation to occur (up to $n^{(\max)} = 4$ bosons per lattice site are allowed in the present study). Periodic boundary conditions along the x and y axes have been used.

2. Mean field

A well known mean-field method to solve the Bose-Hubbard model is the Gutzwiller ansatz [46–49], where the ground-state wave function is assumed to be a tensor product of on-site wave functions:

$$|\Psi\rangle = \bigotimes_j |\psi_j\rangle \text{ where } |\psi_j\rangle = \sum_{n=0}^{N} f_{n,j}|n,j\rangle, \tag{11}$$

where $|n,j\rangle$ represents the Fock state of n atoms occupying the site j, N is a cutoff in the maximum number of atoms per site, and $f_{n,j}$ is the probability amplitude of having the site j occupied by n atoms. For the ground-state property,

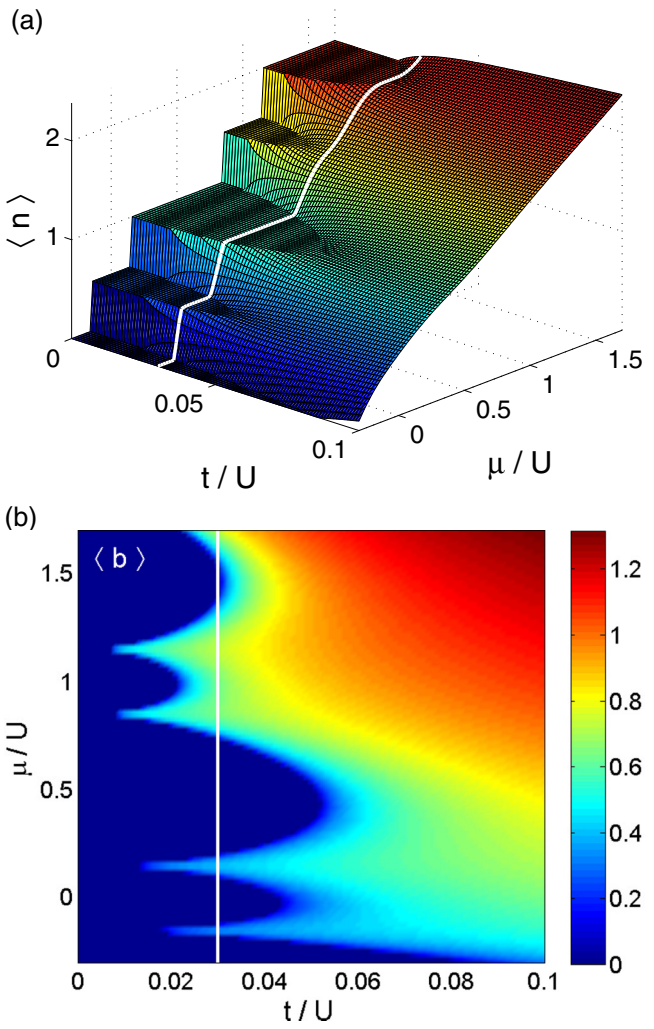

FIG. 3. (Color online) Mean-field phase diagram of the Bose-Hubbard Hamiltonian equation (10) on the honeycomb lattice. (a) Density per site; (b) the superfluid order parameter. The parameters used in the calculation are $t_{1,2,3} = t$, $t_4 = 0$, $\Delta/U = 0.15$, $N = 10$. The white lines correspond to $t/U = 0.03$.

such as the density, the mean-field calculations with a cutoff value $N = 4$ (i.e., the same as the QMC one), give exactly the same results as those in Figs. 3 and 4. However, during the dynamical evolution, Fock states having $n > 4$ could be slightly populated. Therefore, and because it is numerically quite cheap, we have used a cutoff value $N = 10$.

Minimizing the mean-field energy $\langle\Psi|H|\Psi\rangle$ over the amplitudes $f_{n,j}$ allows us to determine the mean-field ground-state properties as functions of the different parameters (U, t, μ_A, μ_B). For instance, the superfluid phase corresponds to a nonvanishing value of the order parameter $\langle\Psi|b_i|\Psi\rangle$, whereas the Mott phase corresponds to a vanishing order parameter and the $|\psi_i\rangle$ are pure Fock states.

In addition, the preceding ansatz (11) can be extended to the time domain giving us access not only to the Bogoliubov excitations above the ground state, but also to the full mean-field evolution of the interacting wave function. More precisely, the time evolution is obtained by solving the following set of

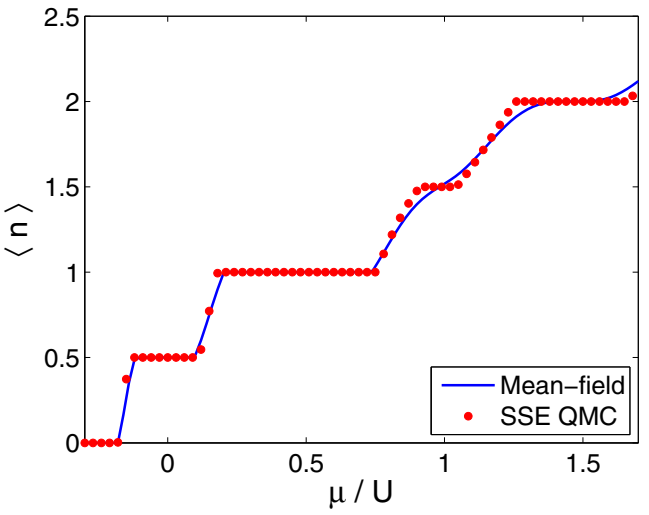

FIG. 4. (Color online) Comparison of QMC and mean-field results for the density per site as a function of total chemical potential $\mu = (\mu_A + \mu_B)/2$. Parameters are $t_{1,2,3} = t, t_4 = 0, \Delta/U = 0.15$, as in Fig. 3, and the hopping amplitude is fixed to $t/U = 0.03$. The blue solid curve is obtained from the mean-field approach (corresponding to the white line in Fig. 3), and the red dots are obtained from QMC simulations. The lattice size for QMC simulations is 16×16, with a maximum atom number per lattice site $n^{(\max)} = 4$. The error bars (not shown) are smaller than the symbols.

equations:

$$i\frac{df_{n,j}(\tau)}{d\tau} = \frac{\partial\langle\Psi(\tau)|H|\Psi(\tau)\rangle}{\partial f^*_{n,j}}. \tag{12}$$

The Bogoliubov excitations are obtained by expanding the amplitudes $f_{n,j}(\tau)$ around their ground-state values $f^{(0)}_{n,j}$, namely,

$$f_{n,j} = \left[f^{(0)}_{n,j} + g_{n,j}(\tau)\right]e^{-i\omega_j\tau}, \tag{13}$$

where ω_j is the frequency of the ground-state evolution. Assuming $|g_{n,j}(\tau)| \ll |f^{(0)}_{n,j}|$ and keeping only the linear terms in the dynamical Eq. (12), one obtains the usual Bogoliubov equations:

$$i\frac{d}{d\tau}\begin{bmatrix} g(\tau) \\ g^*(\tau)\end{bmatrix} = \mathcal{L}\begin{bmatrix} g(\tau) \\ g^*(\tau)\end{bmatrix}, \tag{14}$$

where $g(\tau)$ is a shorthand notation for the vector $(\ldots, g_{0,j}, g_{1,j}, \ldots, g_{N,j}, \ldots)^T$ and $\mathcal{L}$ has the usual Bogoliubov structure:

$$\mathcal{L} = \begin{pmatrix} \mathcal{A} & \mathcal{B} \\ -\mathcal{B}^* & -\mathcal{A}^*\end{pmatrix}. \tag{15}$$

$\mathcal{A}$ and $\mathcal{B}$ are complex matrices satisfying $\mathcal{A}^\dagger = \mathcal{A}$ and $\mathcal{B}^T = \mathcal{B}$.

Due to the $U(1)$ invariance, the values of $f^{(0)}_{n,j}$ can be taken real. Furthermore, as we have observed (see below), the mean-field ground state does not break the translation invariance, such that the values $f^{(0)}_{n,j}$ are the same for all *equivalent* sites, namely, $f^{(0)}_{n,j} = A_n$ for all A sites and $f^{(0)}_{n,j} = B_n$ for all B sites. Because of translation invariance, the Bogoliubov Eq. (14) can be diagonalized in momentum space, taking into account the bipartite nature of the lattice:

$$g_{n,j}(\tau) = \sum_{\mathbf{k}} e^{i(\mathbf{k}\cdot\mathbf{A}_j - \omega\tau)}u_{\mathbf{k},A,n} + e^{-i(\mathbf{k}\cdot\mathbf{A}_j - \omega\tau)}v^*_{\mathbf{k},A,n}, \tag{16}$$

$$g_{n,j}(\tau) = \sum_{\mathbf{k}} e^{i(\mathbf{k}\cdot\mathbf{B}_j - \omega\tau)}u_{\mathbf{k},B,n} + e^{-i(\mathbf{k}\cdot\mathbf{B}_j - \omega\tau)}v^*_{\mathbf{k},B,n} \tag{17}$$

for A sites and B sites, respectively, leading to the following eigensystem:

$$\omega_{\mathbf{k}}\begin{pmatrix} u_{\mathbf{k}} \\ v_{\mathbf{k}}\end{pmatrix} = \mathcal{L}_{\mathbf{k}}\begin{pmatrix} u_{\mathbf{k}} \\ v_{\mathbf{k}}\end{pmatrix}, \tag{18}$$

where $u_{\mathbf{k}} = (u_{\mathbf{k},A,0}, \ldots, u_{\mathbf{k},A,N}, u_{\mathbf{k},B,0}, \ldots, u_{\mathbf{k},B,N})$ and $v_{\mathbf{k}} = (v_{\mathbf{k},A,0}, \ldots, v_{\mathbf{k},A,N}, v_{\mathbf{k},B,0}, \ldots, v_{\mathbf{k},B,N})$. $\mathcal{L}_{\mathbf{k}}$ has the same structure as $\mathcal{L}$, which leads to the usual property: if (u,v) is an eigenstate for the energy ω, then (v^*,u^*) is an eigenstate for the energy $-\omega^*$. Therefore one can focus on the eigenstates with positive skew norm only, i.e., such that $u^\dagger u - v^\dagger v = 1$. The ground state is stable if all these eigenstates have real and positive eigenenergies $\omega_{\mathbf{k}}$.

III. RESULTS

A. Phase diagram

Figure 3 shows the ground-state phase diagram for a honeycomb lattice ($t_4 = 0$) obtained from ansatz Eq. (11). Due to different chemical potentials between the A and B sites, the insulating lobes occur not only at $\langle n\rangle = 0, 1, 2, \ldots$ but also at $\langle n\rangle = 1/2, 3/2, \ldots$. We compare the mean-field result with QMC simulation in Fig. 4, where we plot the density per site as a function of $\mu = (\mu_A + \mu_B)/2$, fixing the hopping amplitude at $t/U = 0.03$, which corresponds to the white lines in Fig. 3. Very good agreement is found between the mean-field approach and QMC simulations, the error bars (not shown) being smaller than the symbols.

B. Excitations

The phase diagram in Fig. 3 itself is not a signature of the Berry curvature induced by the topology of the honeycomb lattice. Indeed, the Hubbard model on the square lattice (i.e., with a nonvanishing hopping parameter t_4) with the same imbalance $\mu_A - \mu_B$ exhibits a similar phase diagram, including the half-integer filling Mott phases. More generally, it is well known that, in the presence of a superlattice, Mott insulating phases can occur for fractional fillings [50–52]. Finally, since the ground state of the Hubbard model corresponds, roughly speaking, to $\mathbf{k} = \mathbf{0}$, precisely where the Berry curvature $\Omega(\mathbf{k})$ vanishes, one does not expect a signature of the Berry curvature in the ground state itself and its impact has to be found in the excitation properties.

As explained above, within the mean-field approach, the Bogoliubov excitations are obtained from the diagonalization of $\mathcal{L}_{\mathbf{k}}$, leading to a band structure for the Bogoliubov spectrum. For instance, in Fig. 5, we show the lowest excitation band for the brick wall lattice for two different phases, namely, the Mott phase ($\mu/U = 0$) and the superfluid phase ($\mu/U = 0.15$). The rest of the parameters are the same as in Fig. 4. As expected, the excitations are gapped in the Mott phase, whereas in the

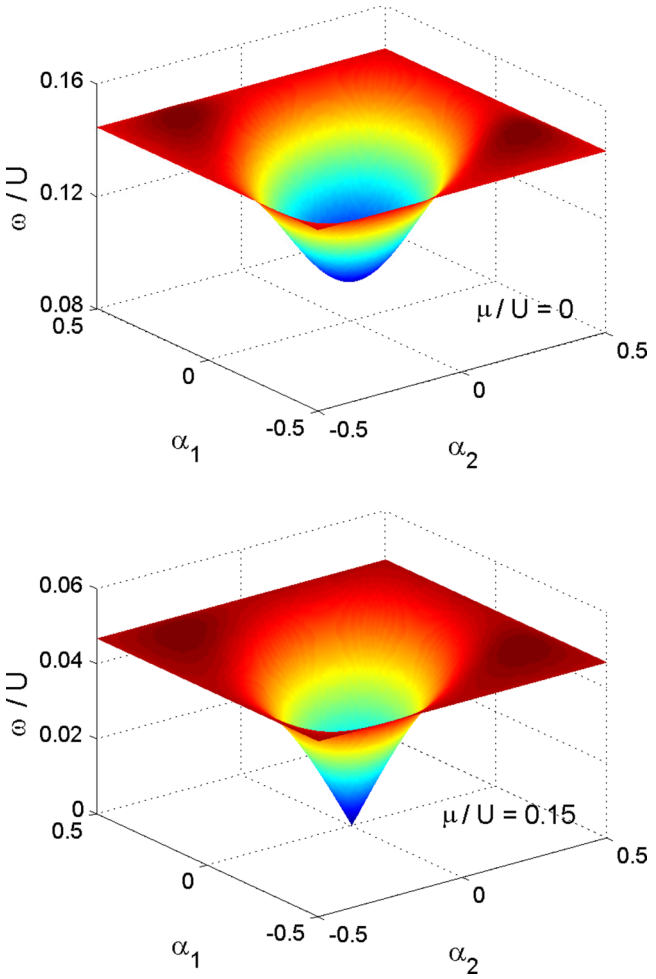

FIG. 5. (Color online) Bogoliubov excitation spectrum $\omega(\mathbf{k})$. Parameters are the same as in Fig. 4. The top panel corresponds to the Mott Phase $\mu/U = 0$ and the bottom one to the superfluid phase $\mu/U = 0.15$. As expected, the excitations are gapped in the Mott phase, whereas in the superfluid phase, they are gapless and exhibit a linear behavior at small momenta.

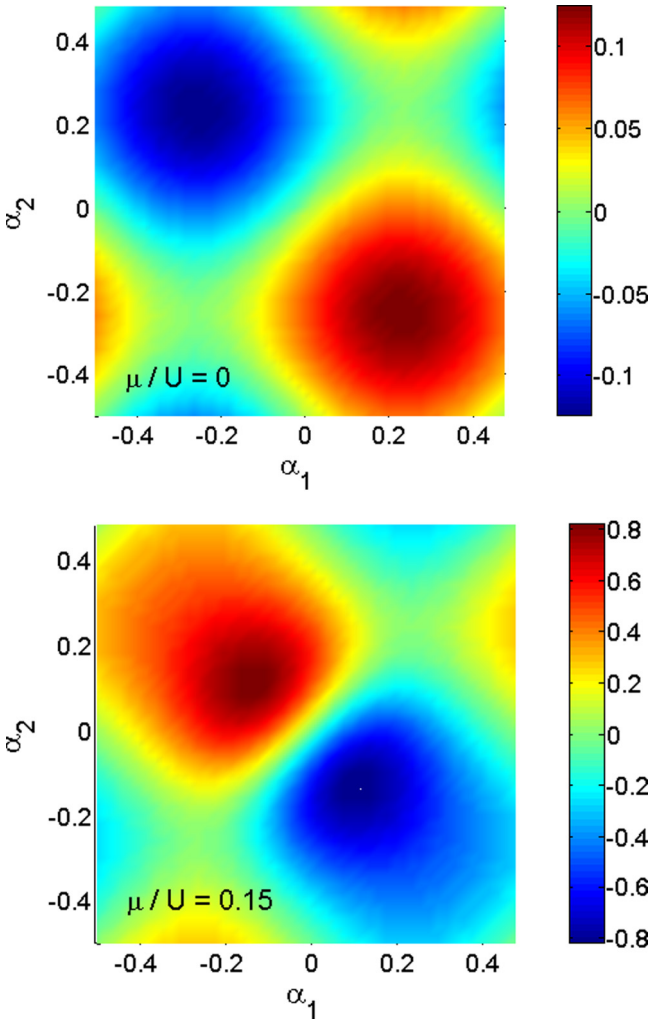

FIG. 6. (Color online) Berry curvature of the Bogoliubov excitations displayed in Fig. 5. One can clearly observe $\Omega(\mathbf{k}) = -\Omega(-\mathbf{k})$ (time-reversal symmetry), the antisymmetry with respect to the diagonal ($k_y \to -k_y$), and the symmetry with respect to the antidiagonal ($k_x \to -k_x$).

superfluid phase, they are gapless and exhibit a linear behavior at small momenta.

In general the Bogoliubov bands are isolated allowing numerical computation [53] of the Berry curvature associated with each band, as shown in Fig. 6, for the two excitation bands of Fig. 5. One clearly sees that in both situations, the Berry curvature is nonvanishing, being maximum (in absolute value) along the antidiagonal, i.e., the k_y axis, like in the noninteracting case. In addition, the time-reversal symmetry and the $y \to -y$ symmetry, like in the noninteracting case, imply that the Berry curvature is odd under both transformations $\mathbf{k} \to -\mathbf{k}$ and $k_y \to -k_y$ and that it is even under the transformation $k_x \to -k_x$. In both Fig. 6 and Fig. 5, these properties are clearly seen: (i) antisymmetric under inversion and with respect to the diagonal; and (ii) symmetric with respect to the antidiagonal.

Similarly, one could define a pseudo Berry curvature for the excitations obtained from QMC computations. However, the QMC does not provide direct access to the effective Hamiltonian governing the excitations, but only to the Green functions. One must note that, in the noninteracting case, the 2×2 structure of $H(k)$ and $G(k,\omega) = [\omega - H(k)]^{-1}$ give rise to the same mapping from the Brillouin zone to the surface of a Bloch sphere (the two angles β and ϕ), and thereby to the same Berry curvature. Hence, we believe that, in the interacting case, the mapping obtained from the 2×2 structure of the Green functions still allows us to define a proper Berry curvature that could be detected through a measure of the Berry phase accumulated adiabatically along a path in the Brillouin zone. For simplicity, we simply use the equal time Green function obtained from the QMC calculation. In $\mathbf{k}$ space, they read

$$\mathbf{G}(\mathbf{k}) = \begin{pmatrix} G_{AA}(\mathbf{k}) & G_{AB}(\mathbf{k}) \\ G_{BA}(\mathbf{k}) & G_{BB}(\mathbf{k}) \end{pmatrix}, \tag{19}$$

where $G_{LL'}(\mathbf{k}) = \langle b^{\dagger}_{\mathbf{k}L} b_{\mathbf{k}L'} \rangle$. Since $\mathbf{G}(\mathbf{k})$ is Hermitian, one can write $\mathbf{G}(\mathbf{k}) = g_0(\mathbf{k})\mathbb{1} + \mathbf{g}(\mathbf{k}) \cdot \boldsymbol{\sigma}$, where $\boldsymbol{\sigma} = (\sigma_x, \sigma_y, \sigma_z)$ are the Pauli matrices. Thereby, one can define the spherical angles $\beta_g(\mathbf{k})$ and $\phi_g(\mathbf{k})$, corresponding to the direction of $\mathbf{g}(\mathbf{k})$, or equivalently, obtained from the diagonalization of $\mathbf{G}(\mathbf{k})$,

similarly to diagonalizing H_0 [see Eqs. (5) and (7)]. From these two angles, one can define a pseudo Berry curvature:

$$\Omega_g(\mathbf{k}) = \frac{1}{2}\left(\frac{\partial \cos\beta_g}{\partial k_x}\frac{\partial \phi_g}{\partial k_y} - \frac{\partial \cos\beta_g}{\partial k_y}\frac{\partial \phi_g}{\partial k_x}\right). \quad (20)$$

This curvature, being computed from the equal-time Green function, is not directly related to a genuine Berry phase that could be measured from the excitations of the system. As explained above, one would need to define a curvature from the real frequency Green function $\mathbf{G}(\mathbf{k},\omega)$. That entails computing the imaginary time Green function and subsequent analytic continuation to the real axis, which is well known to be a delicate task. Therefore, in order to emphasize the impact of the lattice topology on the excitations, we shall focus on the pseudo Berry curvature defined in Eq. (20). The results are shown in Fig. 7 corresponding to a ground state in the $n = 1/2$ Mott phase. For comparison, we also show the pseudo Berry curvature obtained in the same ground state but for the square lattice. In the latter case, the level of the fluctuations of the random pattern is of the order of the numerical accuracy of the QMC results. On the contrary, the curvature for the brick wall lattice is nonvanishing and is largest (in absolute value) around the same position as for the noninteracting case, i.e., around the location of the conical intersections. In addition, this pseudo Berry curvature has the same symmetry properties: $\Omega_g(\mathbf{k}) = -\Omega_g(-\mathbf{k})$ (time-reversal symmetry), odd under $k_y \to -k_y$ and even under $k_x \to -k_x$.

In the superfluid phase, the 2×2 matrix is dominated by its diagonal elements and the resulting pseudo Berry curvature is smaller than the QMC accuracy.

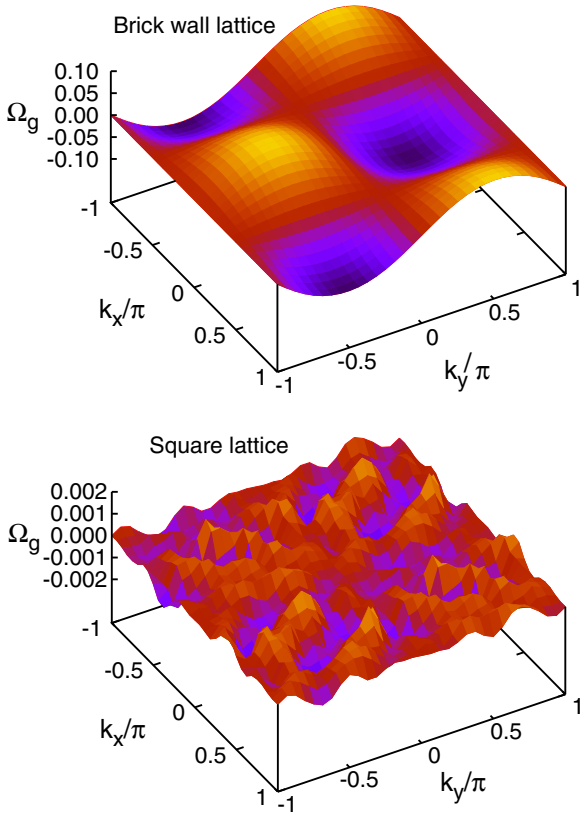

FIG. 7. (Color online) Pseudo Berry curvature, Eq. (20), obtained with the QMC equal-time Green functions for the brick wall and square lattices. The upper panel corresponds to the $n = 1/2$ Mott phase for the brick wall lattice, i.e., $t_{1,2,3} = t$, $t_4 = 0$, $\Delta/U = 0.15$, $\mu/U = 0$, and $t/U = 0.03$. The lower panel corresponds to the $n = 1/2$ Mott phase for the square lattice, i.e., $t_{1,2,3,4} = t$. For the square lattice, one obtains only a random pattern with an amplitude two orders of magnitude lower than the brick wall lattice results; the level of the fluctuations simply reflects the numerical accuracy of the QMC results. This emphasizes that the interacting system must really depict a nonvanishing Berry curvature in the excitation spectrum. In addition, one can see that the pseudo curvature has the same properties as the noninteracting system: it attains the largest (absolute) values around the location of the conical intersections and fulfills $\Omega_g(\mathbf{k}) = -\Omega_g(-\mathbf{k})$, due to the time-reversal symmetry. It is also odd under $k_y \to -k_y$ and even under $k_x \to -k_x$.

IV. ANOMALOUS HALL EFFECT

Although the preceding analysis has shown that the impact of the Berry curvature can be found in the properties of the excitations, one can still raise the question whether it can be observed. It is well known that in this situation, the system is expected to exhibit an anomalous Hall effect (AHE)—a Hall effect without applying an external magnetic field—in the noninteracting case. In this section, we shall demonstrate that one can still observe the AHE in the presence of the interaction. However, the AHE can be observed only if the initial state is a wave packet well localized in real space. Indeed, if one starts with a pure Bloch state, the effect of a constant force only leads to Bloch oscillations, i.e., a periodic variation of the quasimomentum along the direction of the force, and the Berry curvature simply results in a modification of the phase accumulated along the path.

A simple way to prepare a wave packet is to start from the ground state in a harmonic trap, as depicted in Fig. 8: the atoms are well localized in space, still, the wave packet is also well localized in the Brillouin zone around $\mathbf{k} = 0$. The harmonic trap is such that the chemical potential at the center corresponds to the superfluid phase described in the previous section, i.e., $\mu/U = 0.15$ and $t/U = 0.03$. The site energy of the A sublattice is lower than that of the B sublattice, corresponding to $\Delta/U = -0.15$, resulting, in the present case, in a Mott-like state for the A site with a flat density at unit filling (see Fig. 8, top left). On the contrary, the filling of the B sublattice is low, such that the system is in a superfluid phase, with a smooth, Gaussian-like density (see Fig. 8, top right). In both cases, the density in the $\mathbf{k}$ space is peaked at $\mathbf{k} = 0$.

A. Bloch oscillations

To simulate Bloch oscillations, starting from the wave packet, one abruptly removes the harmonic trap and adiabatically increases the linear potential along the y axis at time $\tau = 0$ mimicking the effect of an electric field E along the y axis. The evolution of the wave packet is obtained by solving the time-dependent equations for the mean-field amplitudes, Eq. (12). In $\mathbf{k}$ space, this leads to a smooth evolution of the wave packet (with some broadening) along k_y (see Fig. 9). This is emphasized in Fig. 10, where we have plotted the average value of k_y (within the B sublattice) as as function of time. After the adiabatic transition, the linear increase of

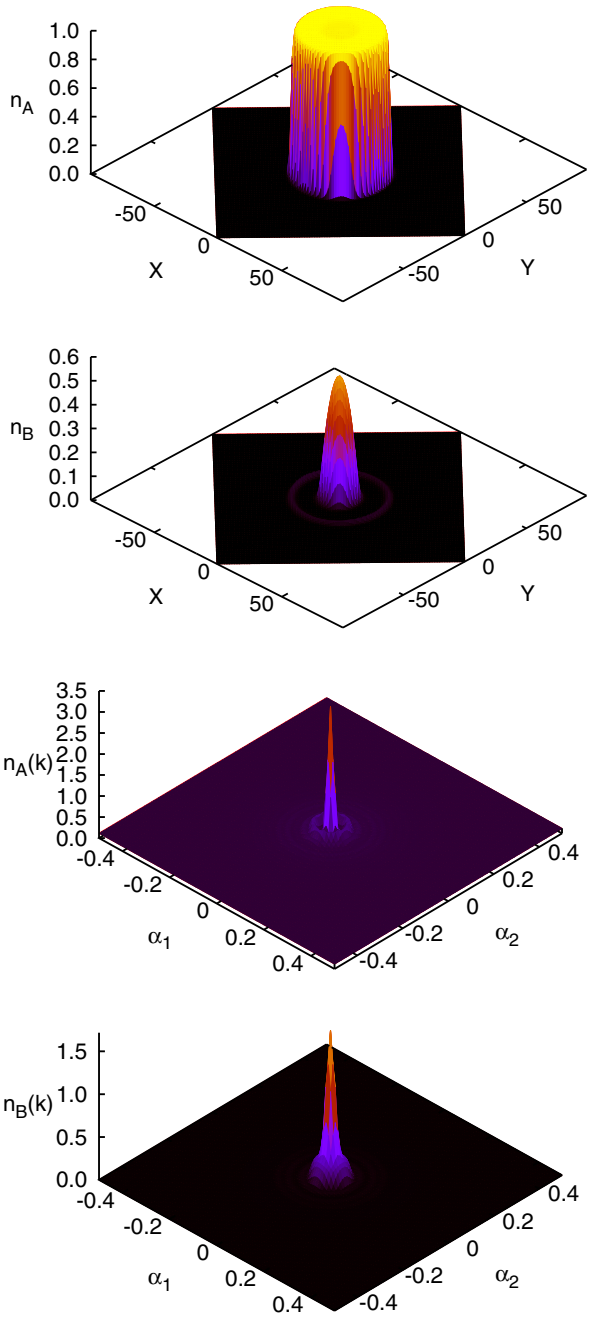

FIG. 8. (Color online) Initial wave packet in a harmonic trap. The atomic density in the A sublattice (respectively, B sublattice) is displayed in the top left (respectively, top right) plot. The harmonic trap is such that the chemical potential at the center corresponds to the superfluid phase described in the previous section. Since the chemical potential μ_A is larger than μ_B, i.e., $\Delta/U = -0.15$, the A sites are in a Mott-like state with unit filling. On the contrary, the filling of the B sublattice is low, such that the system is in a superfluid phase. Densities in the $\mathbf{k}$ space for both the sublattices are displayed in the bottom row and are found to be peaked around $\mathbf{k} = 0$.

k_y with time is a clear signature of the Bloch oscillation. The AHE is demonstrated by the bottom plot in Fig. 10, where we show the displacement from the center of the trap of the wave packet along the x axis, i.e., perpendicular to the applied force. One can clearly see the impact of the Berry curvature, in

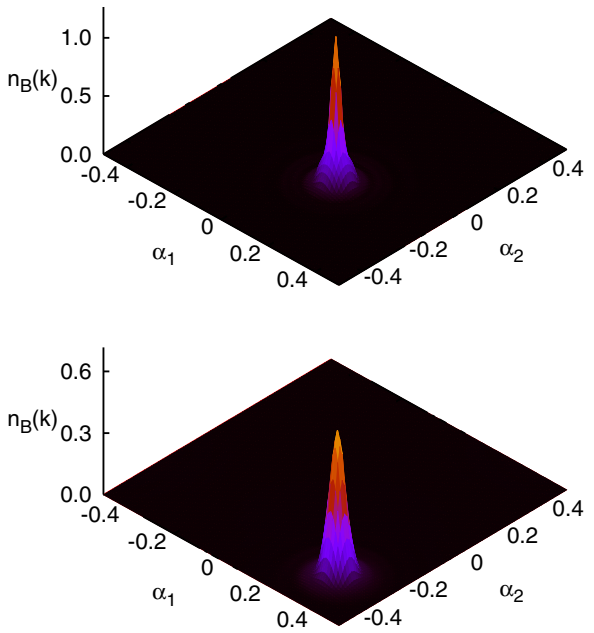

FIG. 9. (Color online) Evolution of the wave packet in momentum space. The upper panel displays the wave packet after a time $\tau = 25/U$, and the lower one after $\tau = 50/U$. The center of the wave packet moves at a constant velocity along the k_y axis, i.e., $\alpha_1 + \alpha_2 = 0$. The broadening of the wave packet is weak.

particular when comparing with a similar evolution but for the square lattice, for which there is no displacement. In addition, changing the sign of the linear potential (i.e., the direction of the applied force), results in changing the direction of the Bloch oscillations $\mathbf{k}(\tau) \to -\mathbf{k}(\tau)$ (i.e., changing the direction of the group velocity of the wave packet). Together with the fact that the Berry curvature is odd with respect to the change $\mathbf{k} \to -\mathbf{k}$, this results in a Hall displacement in the *same* direction along the x axis, as depicted in Fig. 10: the two curves coincide with each other. Note that we have checked that this effect is independent of the exact location of the center of the trap. Finally, we have also verified that if the force is applied along the x axis, no AHE is observed since the Berry curvature vanishes for $k_y = 0$.

B. Shift of the trap center

The amplitude of the AHE discussed above is rather small. One way to get a larger (measurable) effect consists of shifting abruptly the center of the trap at $\tau = 0$ along the y axis, such that the wave packet experiences a net force in that direction. Figure 11 shows the evolution of the expectation value of the center of the wave packet, i.e., $\langle \mathbf{r} \rangle$, after a shift of the trap center by 20 lattice spacings in the y direction. The plot corresponds to a total duration $\tau U = 100$. As one can see, not only does the wave packet evolve along the shifted center, but, at the same time, it moves along the transverse direction, i.e., the x axis. Similarly to the Bloch oscillations, one has the following results: (i) nothing happens on the square lattice; (ii) nothing happens when the shift is along the x axis where the Berry curvature always vanishes; and (iii) the displacement along

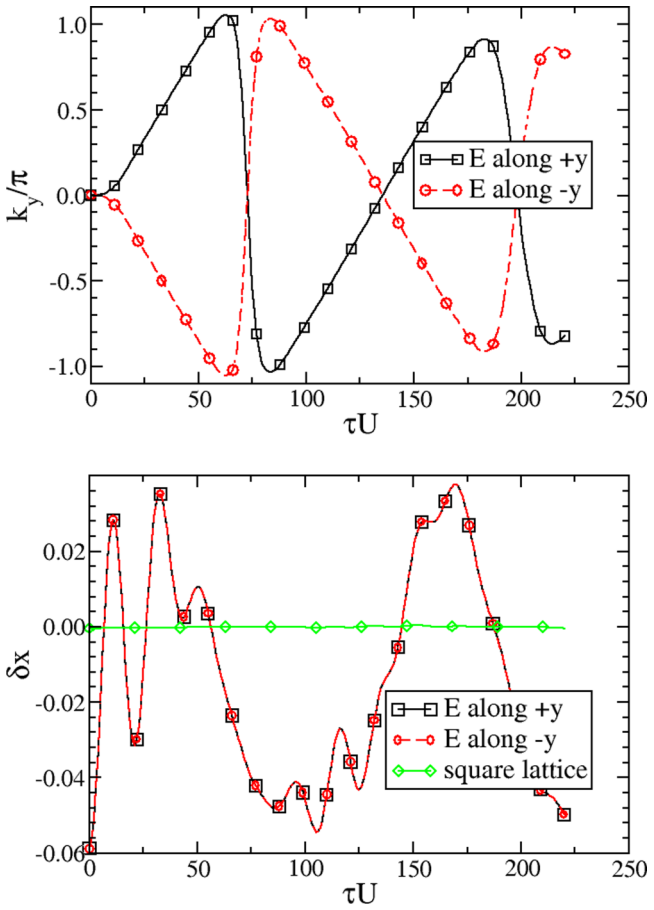

FIG. 10. (Color online) Bloch oscillations and AHE for a wave packet. The top plot shows the average value of k_y (within the B sublattice) as a function of time. After the adiabatic transition, the linear increase of k_y with time is a clear signature of the Bloch oscillation. The two curves, i.e., the continuous (black) line and the dashed (red) line with the circles, correspond to opposite directions of the effective electric field. The AHE is demonstrated by the bottom plot, where one plots the displacement from the center of the trap of the wave packet along the x axis, i.e., perpendicular to the applied force: the continuous (black) line with the squares and the dashed (red) line with the circles correspond to opposite directions of the effective electric field. For comparison, the corresponding displacement on a square lattice is also shown by the continuous (green) line with the diamonds.

x is in the *same* direction whether the trap center is shifted towards the $+y$ or the $-y$ direction.

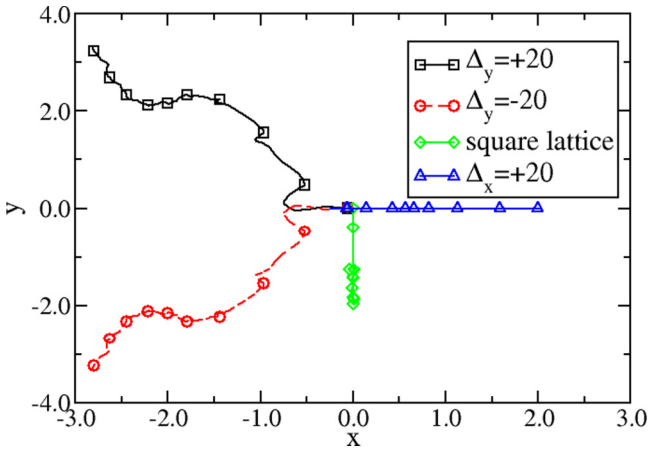

FIG. 11. (Color online) Evolution of the average center of the wave packet, i.e., $\langle \mathbf{r} \rangle$, after a shift of the trap center by 20 lattice spacings in the y direction [continuous (black) line with the squares]. The plot corresponds to a total duration $\tau U = 100$. The wave packet clearly exhibits motion along the transverse direction, i.e., the x axis. Similarly to Bloch oscillations, one has the following results: (i) nothing happens on the square lattice [see the (green) line with the diamonds]; (ii) nothing happens when the shift is along the x axis where the Berry curvature always vanishes [see the (blue) line with the triangles]; and (iii) the displacement along x is in the *same* direction whether the trap center is shifted towards the $+y$ or the $-y$ direction [see the dashed (red) line with the circles].

V. CONCLUSION

In summary, we have shown that for bosons in the brick wall lattice, or equivalently, in the honeycomb lattice, with energy imbalance, the Berry curvature originally seen in the band structure, i.e., for the noninteracting system, is also present in the excitations above the ground state of the interacting system, in both the Mott-insulating phase and the superfluid phase. In addition, we have shown that one consequence of the Berry phase, the anomalous Hall effect, could be observed in dynamical experiments, such as Bloch oscillations.

ACKNOWLEDGMENTS

The Centre for Quantum Technologies is a Research Centre of Excellence funded by the Ministry of Education and National Research Foundation of Singapore. P.S. acknowledges financial support from the Ministry of Education, Singapore via Grant No. MOE2014-T2-2-112. Y.L. acknowledges support from the ARC Discovery Projects (Grants No. DE150101636 and No. DP140103231).

[1] S. Chern, Ann. Math. **47**, 85 (1946).
[2] M. V. Berry, Proc. R. Soc. London, Ser. A **392**, 45 (1984).
[3] J. Zak, Phys. Rev. Lett. **62**, 2747 (1989).
[4] D. J. Thouless, M. Kohmoto, M. P. Nightingale, and M. den Nijs, Phys. Rev. Lett. **49**, 405 (1982).
[5] D. Xiao, M.-C. Chang, and Q. Niu, Rev. Mod. Phys. **82**, 1959 (2010).
[6] X. L. Qi and S. C. Zhang, Rev. Mod. Phys. **83**, 1057 (2011).
[7] R. Resta, J. Phys.: Condens. Matter **12**, R107 (2000).
[8] M. Aidelsburger, M. Atala, S. Nascimbène, S. Trotzky, Y.-A. Chen, and I. Bloch, Phys. Rev. Lett. **107**, 255301 (2011).
[9] G.-B. Jo, J. Guzman, C. K. Thomas, P. Hosur, A. Vishwanath, and D. M. Stamper-Kurn, Phys. Rev. Lett. **108**, 045305 (2012).

[10] L. Tarruell, D. Greif, T. Uehlinger, G. Jotzu, and T. Esslinger, Nature (London) **483**, 302 (2012).
[11] T. Uehlinger, D. Greif, G. Jotzu, L. Tarruell, T. Esslinger, L. Wang, and M. Troyer, Eur. Phys. J. Spec. Top. **217**, 121 (2013).
[12] I. Bloch, J. Dalibard, and W. Zwerger, Rev. Mod. Phys. **80**, 885 (2008).
[13] Y.-J. Lin, R. L. Compton, K. Jimnez-Garca, J. V. Porto, and I. B. Spielman, Nature (London) **462**, 628 (2009).
[14] N. R. Cooper, Phys. Rev. Lett. **106**, 175301 (2011).
[15] M. Aidelsburger, M. Atala, M. Lohse, J. T. Barreiro, B. Paredes, and I. Bloch, Phys. Rev. Lett. **111**, 185301 (2013).
[16] M. W. Ray, E. Ruokokovski, S. Kandel, M. Mttoman, and D. S. Hall, Nature (London) **505**, 657 (2014).
[17] S. Gliga, A. Kákay, R. Hertel, and O. G. Heinonen, Phys. Rev. Lett. **110**, 117205 (2013).
[18] A. Rapp, G. Zarand, C. Honerkamp, and W. Hofstetter, Phys. Rev. Lett. **98**, 160405 (2007).
[19] H. M. Price and N. R. Cooper, Phys. Rev. A **85**, 033620 (2012).
[20] D. Jaksch and P. Zoller, New J. Phys. **5**, 56 (2003).
[21] E. J. Mueller, Phys. Rev. A **70**, 041603 (2004).
[22] A. S. Sørensen, E. Demler, and M. D. Lukin, Phys. Rev. Lett. **94**, 086803 (2005).
[23] N. R. Cooper and J. Dalibard, Europhys. Lett. **95**, 66004 (2011).
[24] M. Atala, Monika Aidelsburger, J. T. Barreiro, D. Abanin, T. Kitagawa, E. Demler, and I. Bloch, Nat. Phys. **9**, 795 (2013).
[25] N. Goldman, E. Anisimovas, F. Gerbier, P. Öhberg, I. B. Spielman, and G. Juzeliūnas, New J. Phys. **15**, 013025 (2013).
[26] K. S. Novoselov, A. K. Geim, S. V. Morozov, D. Jiang, Y. Zhang, S. V. Dubonos, I. V. Grigorieva, and A. A. Firsov, Science **306**, 666 (2004).
[27] A. H. Castro Neto, F. Guinea, N. M. R. Peres, K. S. Novoselov, and A. K. Geim, Rev. Mod. Phys. **81**, 109 (2009).
[28] S.-L. Zhu, B. Wang, and L.-M. Duan, Phys. Rev. Lett. **98**, 260402 (2007).
[29] K. L. Lee, B. Grémaud, R. Han, B.-G. Englert, and C. Miniatura, Phys. Rev. A **80**, 043411 (2009).
[30] Z. Y. Meng, T. C. Lang, S. Wessel, F. F. Assaad, and A. Muramatsu, Nature (London) **464**, 847 (2010).
[31] P. Soltan-Panahi, J. Struck, P. Hauke, A. Bick, W. Plenkers, G. Meineke, C. Becker, P. Windpassinger, M. Lewenstein, and K. Sengstock, Nat. Phys. **7**, 434 (2011).
[32] P. Soltan-Panahi, D.-S. Lühmann, J. Struck, P. Windpassinger, and K. Sengstock, Nat. Phys. **8**, 71 (2012).
[33] T. Uehlinger, G. Jotzu, M. Messer, D. Greif, W. Hofstetter, U. Bissbort, and T. Esslinger, Phys. Rev. Lett. **111**, 185307 (2013).
[34] D. Greif, T. Uehlinger, G. Jotzu, L. Tarruell, and T. Esslinger, Science **340**, 1307 (2013).
[35] K. Gawryluk, C. Miniatura, and B. Grémaud, Phys. Rev. A **89**, 063615 (2014).
[36] K. L. Lee, B. Grémaud, and C. Miniatura, Phys. Rev. A **89**, 043622 (2014).
[37] J. N. Fuchs, F. Piéchon, M. O. Goerbig, and G. Montambaux, Eur. Phys. J. B **77**, 351 (2010).
[38] A. M. Dudarev, R. B. Diener, I. Carusotto, and Q. Niu, Phys. Rev. Lett. **92**, 153005 (2004).
[39] A. W. Sandvik and J. Kurkijärvi, Phys. Rev. B **43**, 5950 (1991).
[40] A. W. Sandvik, and R. R. P. Singh, and D. K. Campbell, Phys. Rev. B **56**, 14510 (1997).
[41] A. W. Sandvik, Phys. Rev. B **59**, R14157 (1999).
[42] P. Sengupta, L. P. Pryadko, F. Alet, M. Troyer, and G. Schmid, Phys. Rev. Lett. **94**, 207202 (2005).
[43] W. Zwerger, J. Opt. B **5**, S9 (2003).
[44] A. Georges, in *Ultracold Fermi Gases*, *Proceedings of the International School of Physics Enrico Fermi, Varenna, 2006, Course CLXIV*, edited by M. Inguscio, W. Ketterle, and C. Salomon (IOS Press, Amsterdam, 2007), p. 477.
[45] C. Trefzger, C. Menotti, B. Capogrosso-Sansone, and M. Lewenstein, J. Phys. B **44**, 193001 (2011).
[46] S. Sachdev *Quantum Phase Transitions* (Cambridge University Press, Cambridge, 2001).
[47] D. Jaksch, C. Bruder, J. I. Cirac, C. W. Gardiner, and P. Zoller, Phys. Rev. Lett. **81**, 3108 (1998).
[48] M. Rigol, G. G. Batrouni, V. G. Rousseau, and R. T. Scalettar, Phys. Rev. A **79**, 053605 (2009).
[49] M. Lewenstein, A. Sanpera, V. Ahufinger, B. Damski, A. Sen(De), and U. Sen, Adv. Phys. **56**, 243 (2007).
[50] V. G. Rousseau, D. P. Arovas, M. Rigol, F. Hébert, G. G. Batrouni, and R. T. Scalettar, Phys. Rev. B **73**, 174516 (2006).
[51] I. Hen and M. Rigol, Phys. Rev. B **80**, 134508 (2009).
[52] I. Hen, M. Iskin, and M. Rigol, Phys. Rev. B **81**, 064503 (2010).
[53] Takahiro Fukui, Yasuhiro Hatsugai, and Hiroshi Suzuki, J. Phys. Soc. Jpn. **74**, 1674 (2005).